Fluidization dynamics of cohesive Geldart B particles. Part II

Pressure fluctuation analysis

Ma, Jiliang; van Ommen, J. Ruud; Liu, Daoyin; Mudde, Robert F.; Chen, Xiaoping; Pan, Suyang; Liang, Cai

DOI
10.1016/j.cej.2019.02.187

Publication date
2019

Document Version
Final published version

Published in
Chemical Engineering Journal

Chemical Engineering Journal 368 (2019) 627–638

Contents lists available at ScienceDirect

Chemical Engineering Journal

journal homepage: www.elsevier.com/locate/cej

Fluidization dynamics of cohesive Geldart B particles. Part II: Pressure fluctuation analysis

Jiliang Ma[a,*], J. Ruud van Ommen[b], Daoyin Liu[a], Robert F. Mudde[b], Xiaoping Chen[a], Suyang Pan[a], Cai Liang[a]

[a] Key Laboratory of Energy Thermal Conversion and Control of Ministry of Education, School of Energy and Environment, Southeast University, Nanjing 210096, PR China
[b] Department of Chemical Engineering, Delft University of Technology, Van der Maasweg 9, 2629HZ Delft, The Netherlands

HIGHLIGHTS

- Pressure fluctuation analysis was used to study the fluidization of cohesive particles.
- Polymer coating was applied to introduce thermal-induced cohesive force.
- Bed changes from multiple-bubbling to single-bubbling regime with increasing cohesion.
- Bubble-promoted operations benefit the whole-bed slugging under strong cohesion.
- Reducing static bed height can repress the whole-bed slugging.

GRAPHICAL ABSTRACT

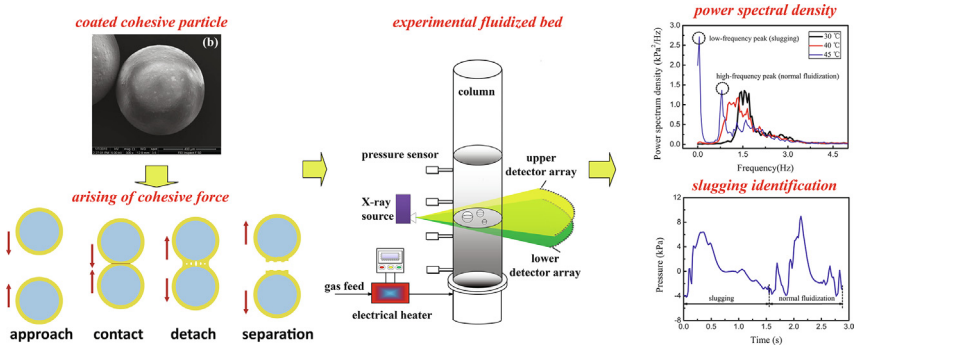

ARTICLE INFO

Keywords:
Cohesive particle
Fluidization
Pressure fluctuation
Slugging
Defluidization

ABSTRACT

The increase of inter-particle cohesive force greatly changes the fluidization dynamics, finally leading to the partial or complete failure of fluidization. However, few studies concern such transition process. This paper investigates the fluidization dynamics of Geldart B particles with a wide-range of cohesive force by analyzing the in-bed pressure fluctuation signals. Combining the bubble information reported in Part I, the local and global fluidization dynamics under different cohesive forces were discussed. The results show that bulk bubble dynamics is weaken with the presence of inter-particle cohesive force. As the force increases, fluidization changes from multi-bubbling regime to single-bubble regime and the factor governing the pressure fluctuation changes from bubble formation to bubble eruption. When the cohesive force is strong, slugging appears near the bed surface, then gradually extends toward the bottom bed by capturing freely fluidizing particles, and finally develops into the whole-bed slugging. At this time, regular fluidization turns into an alternative process between whole-bed slugging and regular status, corresponding to two distinct peaks in power spectral density of pressure signals at 0.1 Hz and 1 Hz respectively. The size of gas slug decreases with the elevation of measurement height. Basically, any operations that promote bubble growth will also facilitate the appearance of whole-bed slugging under strong cohesive force. Reducing the static bed height is a preferable approach to weaken, or even avoid the defluidization of whole-bed slugging, without changing other operational parameters.

* Corresponding author.
E-mail addresses: jlma@seu.edu.cn (J. Ma), J.R.vanOmmen@tudelft.nl (J.R. van Ommen), dyliu@seu.edu.cn (D. Liu), r.f.mudde@tudelft.nl (R.F. Mudde), xpchen@seu.edu.cn (X. Chen), liangc@seu.edu.cn (C. Liang).

https://doi.org/10.1016/j.cej.2019.02.187
Received 20 December 2018; Received in revised form 23 February 2019; Accepted 25 February 2019
Available online 26 February 2019
1385-8947/

Nomenclature

Acronyms

COP	coherent-output power spectral density
IOP	incoherent-output power spectral density
PEA	Poly ethyl acylate
PMMA	poly methyl methacrylate
PSD	power spectral density

Symbols

A_y	average attenuation coefficient of pressure waves
f	frequency (Hz)
f_a	average frequency of power spectral density (Hz)
f_c	cycle frequency (Hz)
$f_{friction}$	friction force (N)
f_{min}, f_{max}	minimum and maximum frequency in power spectral density (Hz)
F_p	Pushing force (N)
H_s	static bed height (cm)
L	number of the segments
n	counter
N	length of pressure signal
N_c	times that the data set crosses the average value
N_s	length of each segment
P_{xy}	cross power spectral density between the time-series pressure signals of x and y (kPa^2/Hz)
P^*_{xy}	conjugate of P_{xy}
P^i_{xx}	power spectral density of each segment (kPa^2/Hz)
P_{xx}	averaged power spectral density (kPa^2/Hz)
t	length of pressure signal in time
t_n	duration of normal fluidization (s)
t_s	duration of slugging (s)
U_g	fluidization gas velocity (m/s)
U_{mf}	minimum fluidization velocity (m/s)
w	window function
x	time-series pressure signal (kPa)
$\_x\_x$	averag value of pressure signal (kPa)
x_i	amplitude of pressure signal (kPa)

Greek letters

σ_p	standard deviation of pressure signal (kPa)
$\sigma_{xy,\ i}$	incoherent standard deviation of pressure signal (kPa)
$\sigma_{xy,\ c}$	coherent standard deviation of pressure signal (kPa)
$\tau_{slugging}$	slugging time fraction
γ^2_{xy}	coherence function

1. Introduction

In many applications of fluidized reactors, the particles are cohesive. Cohesive particles show different fluidization behaviors as compared to non-cohesive system [1], particularly for the highly cohesive bed where sever agglomeration takes place, causing partial or complete failure of fluidization [2,3]. Therefore, it is attractive to obtain more insight into the underlying mechanisms, based on which the processing of cohesive particulate systems could be optimized.

The inter-particle cohesive force studied in this paper mainly refers to liquid bridge force and solid bridge force. Since decades ago, extensive researches have been performed on the fluidization dynamics of such particulate systems for being ubiquitous in industrial applications. Nevertheless, due to the limitation of measurement methods, most of these researches focused on global and visual phenomenon, i.e. minimum fluidization [4,5], defluidization pattern [6], bubble behaviors [7,8], particle mixing [9] etc. Recently, lots of researchers made efforts for more insight into the fluidization dynamics of cohesive particles with the aid of advanced measurement approaches. Che *et al.* applied microwave tomography in a fluidized bed with liquid injection to identify defluidization and to reveal the fluidization regime changes with more liquid content [10]. Boyce *et al.* used magnetic resonance imaging to reconstruct the distribution of particle speed in a fluidization bed with the present of liquid [11]. Savari *et al.* detected the changes in fluidization hydrodynamics with increasing liquid content by means of acoustic emission (AE) [12]. By measuring the conductivity of bed materials, the behaviors of liquid sprayed into a fluidized bed, i.e. liquid content [13], liquid distribution [14,15] and liquid migration between free particles and agglomerates [16,17], have been widely investigated. In the companion work, we reported bubbling dynamics of cohesive Geldart B particles by means of multi-source X-ray tomography analysis [18]. The inter-particle cohesive force was found to facilitate bubble coalescence, leading to an increase in bubble size and decrease in bubble numbers. As the cohesive force increases, the fluidization changes from normal status to an alternative process between normal fluidization and whole-bed slugging. When the cohesive force is strong enough, the fluidization completely fails in terms of stable whole-bed slugging. Note that, X-ray tomography can only reveal bubble information and that the information is only associated with bubbles passing through a given cross section due to the local measurement nature [19]. The perceptions of global fluidization dynamics in such system are still insufficient.

The pressure fluctuation analysis is a promising way to characterize the fluidization dynamics for the advantages of non-intrusive and easy to measure [20]. It can be coupled with other measurement techniques, i.e. acoustic emission (AE) to obtain a comprehensive understanding of the fluidization status [21]. The main challenge for this method is to interpret the signal, because it may be simultaneously influenced by bubble dynamics, bed mass oscillation, particle collisions etc. [22]. Over the past decades, numerous algorithms have been developed to extract the specific dynamic information from the pressure signals, covering bubble behaviors [23–25], fluidization regime transition [26,27] and defluidization [28,29], etc. Basically, these algorithms can be classified as time-domain analysis, frequency-domain analysis and state space analysis. The **time-domain analysis** is to analyze the pressure signal with respect to time, by calculating its standard deviation [30], cycle frequency [31] and Hurst exponent [32], etc. The **frequency-domain analysis** is developed on the basis of Fourier transform that converts a time-series signal into frequency spectrum. By calculating the power spectral density (PSD) [33], coherent- and incoherent-output PSD [24], wavelet coefficients [34,35], etc., periodic fluidization phenomena like bubble evolution, bed mass oscillation and so on are related to different frequency bands. The **state space method** is to characterize the chaotic feature of fluidization system with the aid of non-linear analysis such as attractor reconstruction [36], entropy analysis [27] and correlation dimension [37,38], etc. Detailed instructions for the pressure fluctuation analysis can be found in the comprehensive reviews published by Johnsson *et al.* [39] and van Ommen *et al.* [40].

With the aid of pressure fluctuation analysis, extensive studies have been undertaken to investigate the fluidization of cohesive particles. Silva *et al.* identified the sudden changes in fluidization regime with increasing binder content by examining the mean frequency of Gaussian spectral density [28]. Karimi *et al.* found that the standard deviation of the pressure signal first increases then decreases with the increasing liquid sprayed in bed [41]. Similarly, Bhowmick *et al.* also observed the sharp decline of the standard deviation when large amounts of liquid were injected in bed [42]. Bartels *et al.* used attractor

reconstruction to give an early warning for defluidization [43]. Based on the coherence analysis, Zhou *et al.* found that the bubble size decreases with liquid injection [44]. By examining the standard deviation of pressure signal, they further demonstrated that the bubble growth would be repressed if liquid bridge dominants the liquid behavior, while when liquid evaporation was the main behavior, the liquid would slightly repress, sometimes even facilitate bubble growth [45]. Combining the standard deviation analysis, coherence analysis and wavelet analysis, Shabanian and Chaouki discussed the bubble behaviors under the inter-particle cohesive force of different levels. As the cohesive force increases within a low level, bubble size decreases while bubble passage frequency remains nearly unaffected [46]. At a moderate level of cohesive force, the gas is more prone to pass through the emulsion phase at lower gas velocity while tends to form larger bubbles at higher gas velocity [47]. The presence of a high level of cohesive force results in the formation of much larger bubbles at all gas velocities in bubbling regime [48].

To the authors' knowledge, almost all the studies regarding the influence of inter-particle cohesive force on the fluidization behaviors were performed at the status far from defluidization. Until now, there are few reports about the transition of fluidization dynamics from normal status to defluidization with increasing cohesive force. Obviously, for a better understanding and more targeted optimization of the fluidization dynamics of cohesive particulate systems it is of prime importance to know the inner details of such transition process. Besides that, the companion work (Part I) has reported that the defluidization pattern of the bed under strong cohesive force is whole-bed slugging [18]. Nevertheless, the cause of slugging and the approach for repressing such slugging is still unknown.

In light of this, the objective of the present study is to characterize the influence of inter-particle cohesive force on the global fluidization dynamics of cohesive Geldart B particles by analyzing the in-bed pressure fluctuation signals (hereafter called pressure signal). Combining the bubble information reported in companion work (Part I), we analyzed the transition of the bed from normal fluidization to defluidization with step-wise increment of thermal-induced cohesive force. Since the fluidization fails in terms of whole-bed slugging, the time fraction of slugging over a given period of fluidization was estimated, based on which, the dependence of slugging on operating parameters as well as the approach to repress the slugging were also discussed.

2. Experimental description

The geometric construction of the experimental apparatus and the preparation of cohesive particles have been introduced in the companion work (Part I) [18]. This paper mainly focuses on how to measure and analyze the pressure fluctuation signals.

2.1. Experimental setup

Fig. 1 gives a schematic of the experimental setup. Four probes of 4 mm i.d. and 0.1 m length were in-line installed along the column with a distance of 30 mm, 110 mm, 190 mm and 270 mm from the gas distributor. Each probe was equipped with a wire gauze to prevent the particles from entering the probe. Four gauge pressure sensors of Kistler type 7261 were connected with each probe to measure the in-bed pressure. The charges from the pressure sensors were then transmitted to amplifiers (Kistler amplifier type 5015) and converted to voltage signals sampled by a National Instruments CompactRIO embedded control and acquisition system. The data collection of the pressure signal and the X-ray detector output (Part I) were synchronized with LabView code. The sampling frequency was 1250 Hz. Although the dominant frequency of pressure signals in a bubbling bed is typically below 10 Hz [40], it is still helpful to apply such a high sampling frequency to collect the detailed information of fluidization dynamics [22]. For each case, the pressure data was recorded for 10 min to minimize the influence of random noise.

2.2. Inter-particle cohesive force

The inter-particle cohesive force was introduced by coating the inert base particles with polymer layer. Table 1 lists the properties of the base particles. The minimum fluidization gas velocity was measured at ambient pressure and room temperature of 25 °C. The polymer layer was the solidification outcome of mixed solution (commercial name, Eudragit NE30D) of Poly ethyl acrylate (PEA) and poly methyl methacrylate (PMMA) around particle surface. In this work, the polymer layer thickness was controlled around 10 μm. It is very thin relative to the diameter of base particles, so the influence of the layer on particle size could be neglected.

For the present work, the cohesive force arises during the collision between two coated particles at a temperature over the glass transition state [49], as shown in Fig. 2. Upon contact, the surface of polymer layer deforms and polymer chains move across the interface. The interdiffusion between polymer chains is closely related to the

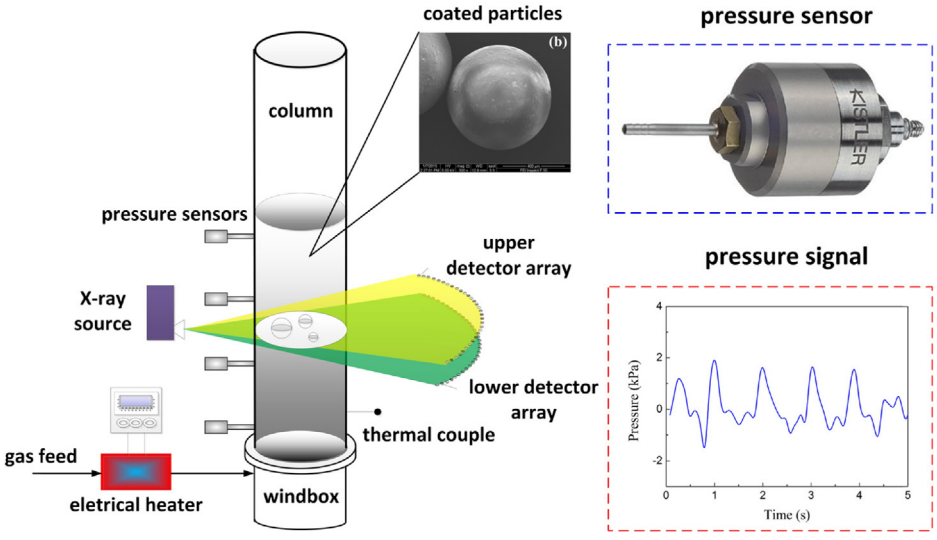

Fig. 1. Schematic of experimental setup.

Table 1
Properties of base particles.

item	value	unit
species	glass beads	–
diameter	600	μm
density	2500	kg/m^3
minimum fluidization velocity	0.325	m/s

temperature. As the particles detach, a solid bridge forms between particles with the entanglement of polymer chains, during which the inter-particle cohesive force arises. When the particles completely separate, the solid bridge ruptures and the cohesive force disappears correspondingly. For the polymer layer used in the present work, it is possible to adjust the cohesive force over a wide range by changing the temperature within a narrow range close to ambient [50]. Bouffard *et al.* found that the cohesive force between two coated particles increases almost linearly with the particle temperature, and proposed equations to predict the cohesive force [51]. Based on the equation, the inter-particle cohesive force for the present work was roughly estimated. As the temperature increases from 25 °C to 45 °C, the cohesive force increases from 2.5 to 6 times particle gravity. Interested readers can go through the reference [51] for detailed information about the polymer layer property.

3. Data analysis

3.1. Time-domain analysis

Analyzing the standard deviation of pressure signals is usually the first choice prior to other methods, for its simplicity and suitability to detect dramatic changes of fluidization [42]. It has been widely used in determining the minimum fluidization velocity [30,52], defluidization [42,53] and regime transition [26,54], etc. Its definition is as follows:

$$\sigma_p = \sqrt{\frac{1}{N-1}\sum_{n=1}^{N}(x(n)-\bar{x})^2} \tag{1}$$

where $x(n)$ is the discrete data of the pressure signal, $\bar{x}$ the average value of $x(n)$, N the number of data points. The main drawback of the method is that the analysis cannot distinguish different dynamical information and that it strongly depends on the fluidization gas velocity which, however, usually fluctuates in industrial processes.

Cycle frequency is an effective tool for detecting the apparent change of fluidization behaviors as well as the particle size distribution [31]. It is the number of times that a time-series pressure signal crosses its average value per second:

$$f_c = \frac{N_c}{t} \tag{2}$$

where N_c is the times for the signal crossing its average value and t is the signal length in time.

3.2. Frequency-domain analysis

Frequency-domain analysis is a useful tool for distinguishing different types of fluidization behavior, because the information of dynamical sources is usually encoded in different frequency bands [55]. Among different frequency-domain methods, the power spectral density (PSD) of the signal is the most used one. It is calculated by dividing the whole signal into L segments with individual length of N_s, then applying Fast Fourier Transformation to each segment:

$$P_{xx}^{i}(f) = \frac{1}{\sum_{n=1}^{N_s} w^2(n)}\left|\sum_{n=1}^{N_s} x_i(n)w(n)\exp(-j2\pi fn)\right|^2 \tag{3}$$

where $x_i(n)$ is the ith segments of the entire pressure signal, $w(n)$ is the window function. In the present work, we chose the Hamming window as the window function. By averaging the spectrum over L segments, the mean power spectral density becomes:

$$P_{xx}(f) = \frac{1}{L}\sum_{n=1}^{L} P_{xx}^{i}(f) \tag{4}$$

The average frequency, f_a is the frequency that divides the energy of the PSD into two equal parts [56]. Unlike the dominant frequency that corresponds to the highest intensity of the PSD, f_a accounts for all the waves based on their amplitudes, and is therefore very representative for characterizing the PSD with broad frequency band and multiple peaks. Its definition is as follows:

$$\int_{f_{\min}}^{f_a} P(f)df = \int_{f_a}^{f_{\max}} P(f)df \tag{5}$$

where $P(f)$ is the intensity of PSD at the frequency of f; f_{min} and f_{max} are the minimum and maximum frequency of PSD.

Besides bubbles, bed mass oscillations, gas turbulence, bubble interaction, etc. will also contribute to the PSD as independent peaks, which poses challenges for further interpretation of the pressure signal [57]. Coherence analysis is thus developed to distinguish these phenomena based on the fact that the phenomena cause different similarities in the pressure signals at different locations. The analysis was undertaken by calculating the coherence function between the in-bed pressure signal and the reference signal collected in the wind box, then deriving the coherent-output PSD (COP) and incoherent-output PSD (IOP) [20]. The coherence function between two pressure signals is calculated as:

$$\gamma_{xy}^2(f) = \frac{P_{xy}(f)P_{xy}^*(f)}{P_{xx}(f)P_{yy}(f)} \tag{6}$$

where $P_{xx}(f)$ and $P_{yy}(f)$ are the PSD of the pressure signals collected in the wind box (reference signal) and other in-bed positions respectively. $P_{xy}(f)$ is the cross PSD between $P_{xx}(f)$ and $P_{yy}(f)$; $P_{xy}^*(f)$ is the conjugate

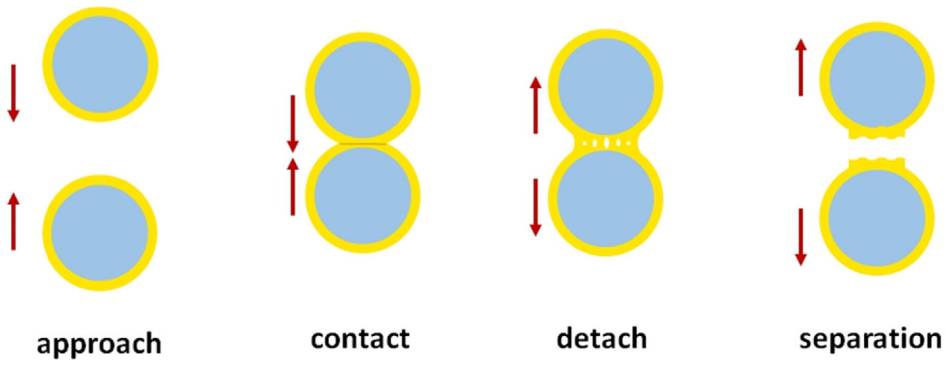

Fig. 2. Collision of two coated particles.

of $P_{xy}(f)$. Based on the coherence function, the definitions of COP and IOP are given:

$$\mathrm{COP}(f) = \gamma_{xy}^2 P_{yy} \tag{7}$$

$$\mathrm{IOP}(f) = (1 - \gamma_{xy}^2) P_{yy} \tag{8}$$

COP is related to the pressure waves induced by bubble coalescence, gas flow fluctuations, bubble eruption, and bed mass oscillation. The pressure wave travels upward with linear attenuation and downward with constant amplitude. IOP represents the incoherent components between the two signals, which relates to the local phenomena without transmitting features, such as bubble passage and local turbulence.

According to the Parseval's theorem, the standard deviation of the coherent and incoherent components of pressure signals can be calculated as:

$$\sigma_{xy,i}^2 = \int_0^\infty \mathrm{IOP}(f)df \tag{9}$$

$$\sigma_{xy,c}^2 = \int_0^\infty \mathrm{COP}(f)df \tag{10}$$

$\sigma_{xy,i}$ characterizes the amplitude of pressure signals caused by the incoherent components. The ratio of $\sigma_{xy,\,c}$ to the standard deviation of the reference signal σ_x (named as A_y) is the average attenuation coefficients of pressure waves:

$$A_y = \frac{\sigma_{xy,c}}{\sigma_x} \tag{11}$$

4. Results and discussion

Fig. 3 plots an example of the time-series pressure signals measured at different heights. The signals are 5 s in length and randomly cut out from the signals of 10 min. Generally, the pressure signal shows an oscillatory nature, indicating the feasibility of the analysis with frequency-based methods. The fluctuation of the pressure signals at different heights follow similar trend, only with certain shift in time. This means that the fluctuation of the pressure signals are mainly caused by some coherent phenomena. Despite the similarity in the global trend, there also exist deviations in some details of the pressure signals. This implies that incoherent phenomena, i.e. bubble passage or local turbulence, also contribute to the pressure fluctuations.

4.1. Time-domain analysis

Fig. 4 shows the standard deviation of pressure signals σ_p at different heights and cohesive forces. With the elevation of the measurement heights, σ_p remains nearly unchanged till 110 mm, beyond which it starts to decrease. This is attributed to the decreasing bubble-interaction with the increasing measurement height. Similar trends were also observed by Zhang *et al.* [58]. As the bed temperature increases below 35 °C, a tiny increase of σ_p is observed, indicating a slight increase in the bubble size, which agrees well with the companion work (Part I) [18]. When the temperature exceeds 35 °C, σ_p sharply increases then decreases for the measurement heights of 30 mm, 110 mm and 190 mm while rises monotonically for 270 mm. The initial increase of σ_p between 35 °C and 40 °C is caused by the presence of slugging that greatly enhances the averaged bubble size. The decline of σ_p beyond 40 °C is difficult to interpret. Bhowmick *et al.* reported similar results when injecting large amounts of liquid into the bed [42]. They ascribed it to the decline of bed fluidity but did not give a detailed explanation.

Fig. 5 shows the effects of static bed height H_s on σ_p under different cohesive forces. The signal is recorded at the height of 110 mm. Generally, the higher H_s is, the larger σ_p could be observed because the total number of bubbles increase with H_s, which enhances the bubble-interaction, leading to an increase in the signal amplitude [35]. Moreover, bubble interaction is more sensitive to the cohesive force at large H_s, as the growth rate of σ_p at H_s = 400 mm is much larger than the other three cases. According to the bubbling bed theory, the bed with static height of 400 mm has larger bubbles at the bed top due to increasing bubble coalescence. Besides, the presence of cohesive force increases the bubble size as revealed in Part I. Therefore, it is more prone to induce slugging and thus give rise to larger σ_p for H_s = 400 mm. The effects of static bed height on the slugging characteristics will be discussed in detail hereafter.

4.2. Frequency-domain analysis

Fig. 6 plots the power spectral density (PSD) of the pressure signals measured at different heights and cohesive forces for $U_g = 2.5U_{mf}$. At 30 °C, the PSD curve generally shows a mono-modal distribution with the dominant frequency around 1.5 Hz which is usually considered as the natural oscillation frequency of the bed [23,59]. Despite the dominant peak, some distinct peaks with less intensity were also observed. The broad band of peak frequencies corresponds to the rupture of large bubbles or the formation of small bubbles [27,35]. As the cohesive force increases, the curve shifts toward lower frequency owing to the decreasing bubble numbers. When the cohesive force is strong (45 °C), the whole-bed slugging takes place. A strong periodicity of piston-like movement of the bed as a whole and normal bubbling fluidization are observed. Different from non-cohesive bed in which the PSD has a distinct and narrow-bandwidth peak when slugging occurs [23,33], the present PSD behaves bi-modal distribution at 45 °C, with two dominant peaks at 0.1 Hz and 1 Hz. According to Part I, it can be assumed that the two peaks correspond to the whole-bed slugging and normal fluidization respectively.

4.2.1. Normal fluidization.

As the cohesive force increases, the band width of the peaks corresponding to the normal fluidization (high-frequency peak) decreases, indicating that the normal fluidization changes from multi-bubbling regime [39] to single-bubbling regime [60]. With the increasing cohesive force, the peak intensity for normal fluidization slightly rises at the measurement height of 30 mm and 110 mm (Fig. 6(a) and (b)) while sharply increases at 190 mm and 270 mm (Fig. 6(c) and (d)), implying that the size of normal bubbles considerably rises in the vicinity of bed surface. It is worth pointing out that our companion work (Part I) reported different behaviors that the average size of 'bubbles' near the bed surface changes slowly with the cohesive force [18]. The difference may be attributable to the presence of gas slugs (its definition has been given in Part I) under strong cohesive force, because X-ray tomography used in Part I captures both normal bubbles and gas slugs. The

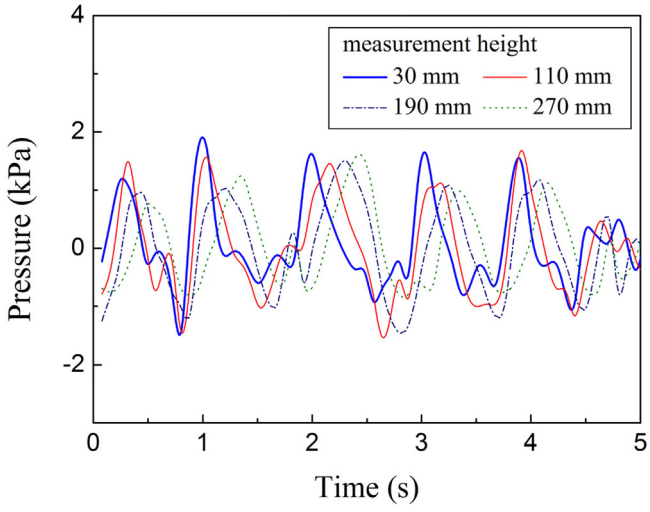

Fig. 3. Example of time-series pressure signals at different heights.

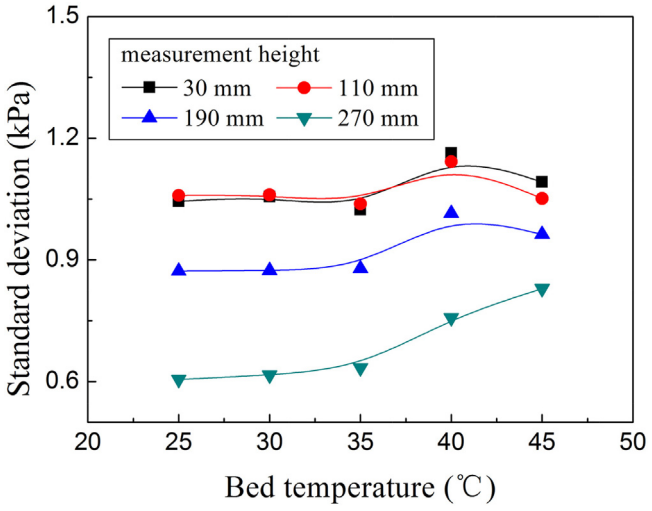

Fig. 4. Standard deviation of the pressure signals at different heights and cohesive forces for $U_g = 2.5U_{mf}$ and $H_s = 300$ mm.

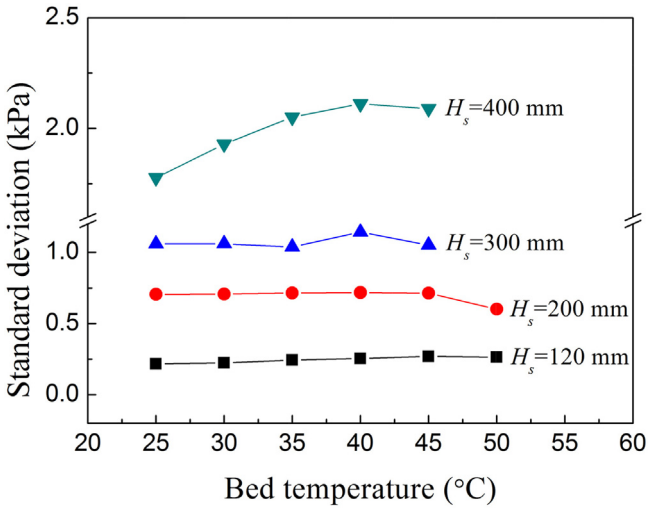

Fig. 5. Effects of static bed heights on the standard deviation of pressure signals measured at 110 mm and different cohesive forces.

comparison between the two works reveals that the size of gas slug decreases with the elevation of measurement height, which thus lowers the 'averaged' bubble size.

4.2.2. Slugging.

The intensity of the peaks for slugging increases with the cohesive force, indicating the growth of slug. With the increasing cohesive force, the slugging intensity increases, indicating the growth of slug size. As shown in Fig. 6(a), the slugging has an intensity much larger than normal fluidization, implying that in the bottom bed the size of gas slugs is larger than normal bubbles. The difference between the two peaks decreases with the elevation of the measurement height, due to the decrease in slug size and the increase in normal bubble size. The dependence of slugging characteristics on the operational conditions will be discussed in the Section 4.3.

Fig. 7 presents the average frequency of pressure signals, f_a as a function of the cohesive force at different heights. As seen, f_a decreases with the elevation of measurement height, because large bubbles, presenting at higher heights, increase the bubble-passage induced components that usually concentrated in the low-frequency range [61], thus leading to the decline of f_a. Similarly, the enhanced bubble coalescence by the cohesive force also increases the bubble-passage components, thereby causing the initial decrease of f_a. Note that the decreasing rate of f_a is relatively small before 35 °C, implying that the influence of the cohesive force on the bubble coalescence is quite limited, which is consistent with the results reported in Part I. As the bed temperature exceeds 35 °C, f_a sharply decreases owing to the presence of low-frequency slugging that shifts the energy distribution of pressure signals to the lower frequency. The continuous decline of f_a indicates that the slugging gradually dominates the fluidization with increasing cohesive force.

Coherence analysis is a favorable approach to interpret PSD by estimating the coherent characteristics between adjacent pressure signals. The first step for applying the analysis is to determine the reference signal. In this paper, we used the pressure signal at 30 mm height, instead of that in the wind box, as the reference signal. Fig. 8 compares both signals measured at 30 mm and wind box. As seen, the pressure signals are generally overlapped, although slight deviations still exist in some details. This shows that adopting the pressure signal at 30 mm as the reference signal is feasible.

Fig. 9 plots the effects of the cohesive force on the coherent-output PSD (COP) and incoherent-output PSD (IOP) of the pressure signals at different heights. Generally, the peaks in both PSD (Fig. 6) and COP (Fig. 9) are almost coincident. This indicates that the pressure fluctuation is mainly determined by the pressure waves created in bed. As the cohesive force increases, the peaks in COP and IOP both shift toward lower frequencies, implying the reduction in bubble behaviors, i.e. the formation, interaction and eruption of bubbles (COP) and local bubble passage (IOP) [25,62].

The high-frequency peaks in COP are hardly observed in IOP for all the cohesive cases, indicating that these peaks correspond to the fast-travelling pressure waves. As reported by van der Schaaf *et al.*, upward traveling pressure wave coincides with the bubble formation at gas distributor, whose amplitudes decrease linearly with the distance from the point of origin, and downward traveling wave corresponds to bubble eruption at bed surface, whose amplitudes keep unchanged in the downward direction [20,62]. As shown, at 30 °C and 40 °C the intensity of the high-frequency peak of COP decreases with the elevation of the measurement height (Fig. 9(a), (c) and (e)), suggesting that the pressure fluctuation is mainly controlled by the bubble formation. When the bed temperature equals 45 °C, the intensity is independent of the measurement height. This means that the pressure fluctuation is controlled by the bubble eruption.

The whole-bed slugging presents in both COP and IOP as the low-frequency peak at 0.1 Hz. In COP, this peak is attributed to the eruption of gas slug [63], and in IOP it represents the passage of gas slug [62]. With the increasing measurement height, the intensity of the low-frequency peak of COP decreases (Fig. 9(a), (c) and (e)). As for IOP, the intensity increases with the height (Fig. 9(b), (d) and (f)). This is related to the dynamical feature of the slugging.

Fig. 10 shows a schematic of the whole-bed slugging. When the cohesive force is large enough, the bubbles increase to considerable sizes similar to the bed dimension. Slugging appears at this moment in the vicinity of bed surface and gradually extends downward by capturing the freely fluidizing particles through cohesive force. Finally, the whole-bed slugging takes place as all the particles form one particle slug and a piston-like movement of the bed as a whole was observed. During the rising, the particle slug experiences the pushing force from the fluidizing gas, F_p and the friction force with the column wall, F_f. The combination of the two forces continuously peels off the particles, finally causing the breakage of the slug. Therefore, the survival probability of the particle slug decreases as it rises. As introduced previously, the low-frequency peak in COP is attributable to the eruption of gas slugs, which motivates pressure waves attenuating linearly when travelling upward. Therefore, the intensity of slugging peak in COP decreases with the increasing measurement height (Fig. 9(a), (c) and (e)). Similarly, the decreasing survival probability of gas slug with measurement height leads to an increase in the incoherent component

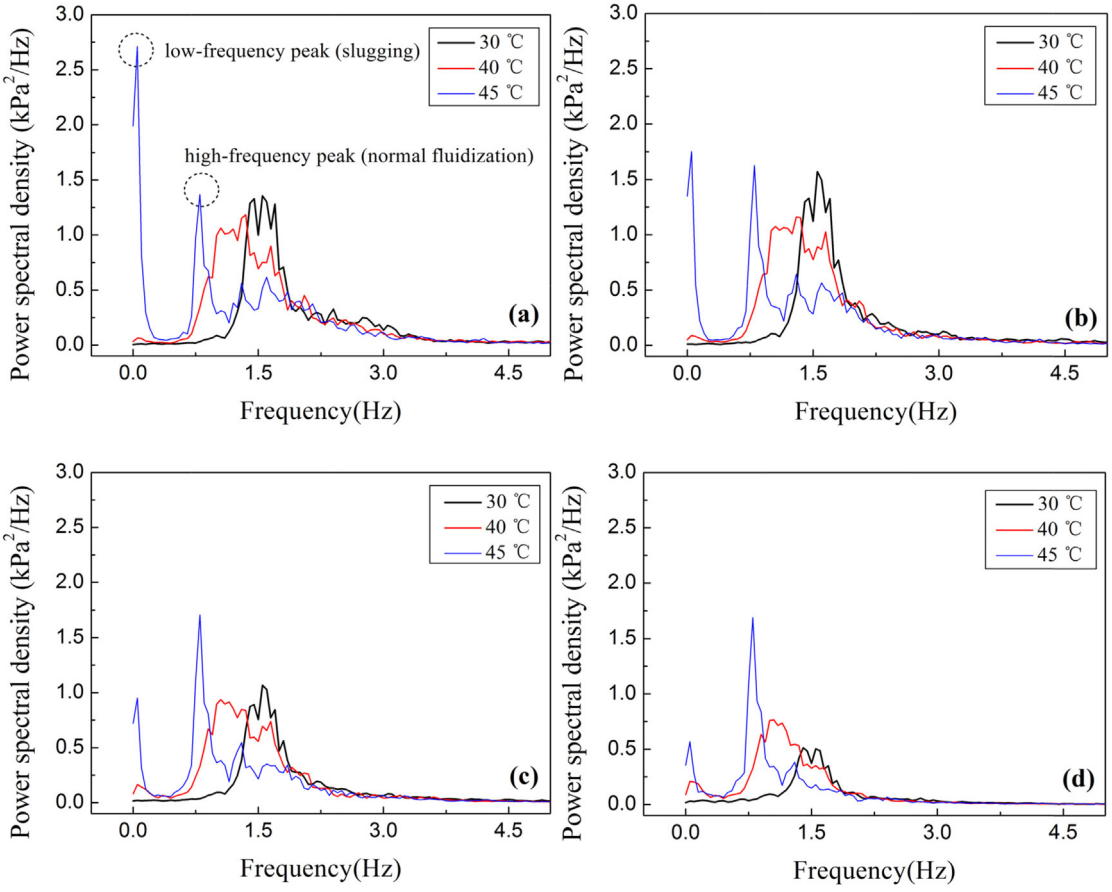

Fig. 6. Effects of cohesive force on the Power spectral density of pressure signals measured at the heights of (a) 30 mm, (b) 110 mm, (c) 190 mm, (d) 270 mm for $U_g = 2.5U_{mf}$.

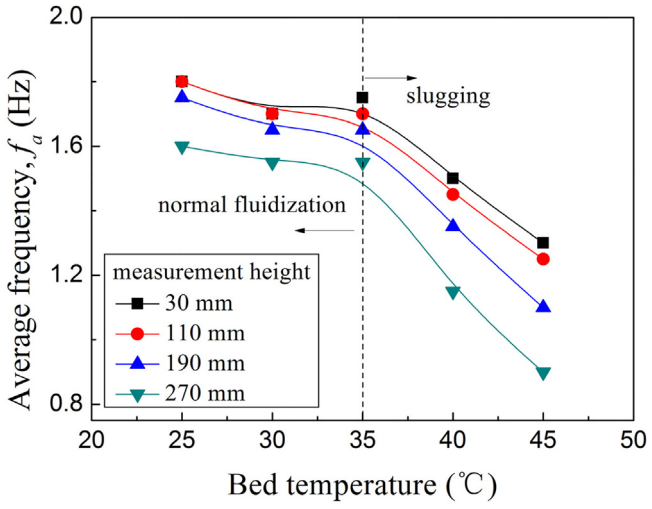

Fig. 7. Average frequency of pressure signals as a function of cohesive force at different heights for $U_g = 2.5U_{mf}$ and $H_s = 300$ mm.

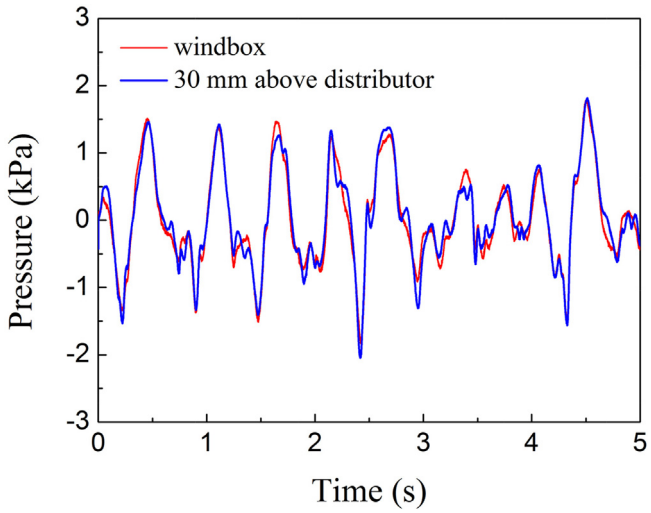

Fig. 8. Comparison between the pressure signals at 30 mm height and that in the wind box.

of pressure signals, thereby resulting in higher IOP (Fig. 9(b), (d) and (f)).

Fig. 11 shows the attenuation coefficients of pressure waves along the bed height under different cohesive forces. It is calculated according to Eq.(11) and reflects the attenuating characteristics of pressure wave amplitude. Generally, the coefficient decreases with the elevation of the measurement height, behaving a typical transmitting feature of the upward-traveling pressure waves [62]. And, the coefficient is found to be larger at $U_g = 2U_{mf}$ (Fig. 11(a)) than $U_g = 3U_{mf}$ (Fig. 11(b)). This is because the pressure waves can be seriously attenuated in the beds with large bubble volume fraction [46,64]. As the fluidization gas velocity increases, more gas is present as bubbles, thus enhancing the bubble volume fraction as well as the pressure wave attenuation. The attenuation coefficients are nearly the same for the temperature of 30 °C and 40 °C at all heights. For both cases, as previously discussed, the pressure fluctuation is closely related to the pressure waves caused by

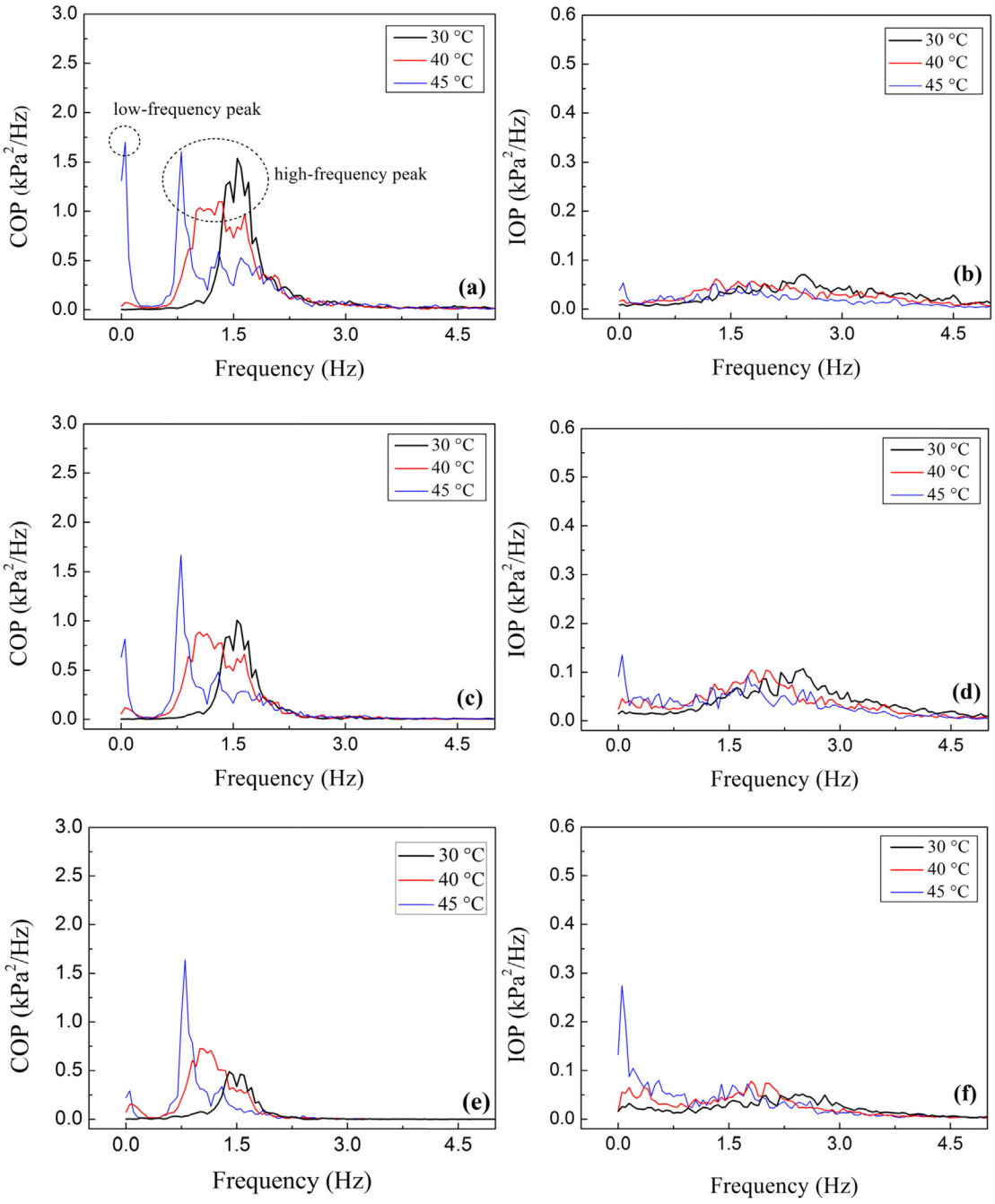

Fig. 9. Effects of cohesive force on the coherent-output PSD (COP) and incoherent-output PSD (IOP) of the pressure signals at different heights for $U_g = 2.5U_{mf}$, $H_s = 300$ mm. (a)-(b): 110 mm; (c)-(d): 190 mm; (e)-(f): 270 mm.

bubble formation. And, the results of X-ray tomography analysis (Part I) reveal that the size of newly formed bubbles changes little with the cohesive force prior to 40 °C [18]. Therefore, the attenuation coefficients for both 30 °C and 40 °C are similar. Note that, a different trend was observed concerning the case of 45 °C. Similar unexpected decay of pressure wave amplitude has ever been reported, although the underlying mechanisms are still in controversy. Musmarra *et al.* attributed it to the chaotic particle contact [65]. Bi *et al.* explained it on the basis of the self-oscillation of particles [66]. For the present work, the unexpected attenuation of pressure wave amplitude at 45 °C should be related to the whole-bed slugging. It leads to the non-uniform distribution of bed voidage throughout the bed, which results in the different attenuation behavior of pressure waves [62].

Fig. 12 shows the effects of fluidization gas velocity and cohesive force on the incoherent standard deviation, $\sigma_{xy,i}$ of signals at different heights. $\sigma_{xy,i}$ is mainly controlled by the passage of bubbles and therefore is usually used to estimate the size of bubbles [20]. As seen, $\sigma_{xy,i}$ increases with the fluidization gas velocity, because the size of bubbles keeps increasing, which generates more incoherent component in the pressure signal as the bubbles pass by the pressure probe. With the increasing cohesive force, $\sigma_{xy,i}$ decreases at the gas velocity smaller than 0.85 m/s but increases at larger velocities. Similar trends are observed concerning the signals collected at different heights. According to Parseval's theory, $\sigma_{xy,i}$ gives information on the energy of pressure fluctuation caused by rising gas bubbles [20]. As reported in Part I, bubble frequency decreases as the cohesive force increases. Therefore, the reduction in the bubble numbers will cause the decline of the incoherent standard deviation. As the fluidization velocity further

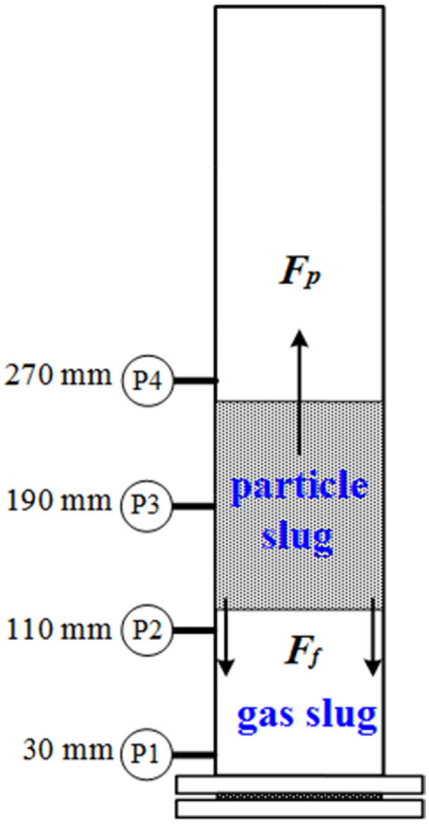

Fig. 10. Schematic of the whole-bed slugging.

increases, the bubble size keeps increasing, prone to trigger slugging in the vicinity of bed surface. The slugging gradually extends toward bed bottom with the aid of the inter-particle cohesive force and finally forms the whole-bed slugging. It is worth pointing out that, besides the bubble size, the incoherent component of pressure signal is also related to the bed mass presenting above the bubble [20]. During the whole-bed slugging, the whole bed mass imposes on the gas slug. Therefore, the passage of gas slug leads to an incoherent standard deviation much larger than normal bubbles. As will be discussed later, the time fraction of the whole bed slugging increases with the cohesive force, especially at large fluidization velocity. Consequently, the incoherent standard deviation increases with cohesive force at larger velocities.

4.3. Slugging characteristics

As previously revealed, slugging is the major form for the de-fluidization under strong cohesion and is also the main cause of the dramatic change of pressure signals. In the following, we will explore the relationship between the operating parameters and the slugging characteristics, then further discuss the approach to weaken or even avoid slugging.

Fig. 13 plots a fragment of pressure signal collected at the bed temperature of 45 °C, $U_g = 2.5U_{mf}$, $H_s = 400$ mm and the measurement height of 30 mm. Both slugging and normal fluidization are present in this period. As seen, these two status correspond to the signal curves with different flatness, slugging being relatively flat while normal fluidization being more fluctuant. Cycle frequency, f_c whose definition has been given in Eq.(2), is usually used to characterize the signal flatness based on which the changes of fluidization regime can also be detected [67]. With the aid of the synchronized X-ray tomography, we estimate the cycle frequency to be less than 2 Hz when slugging takes place. Therefore, 2 Hz is identified as the threshold value to distinguish the slugging and normal fluidization.

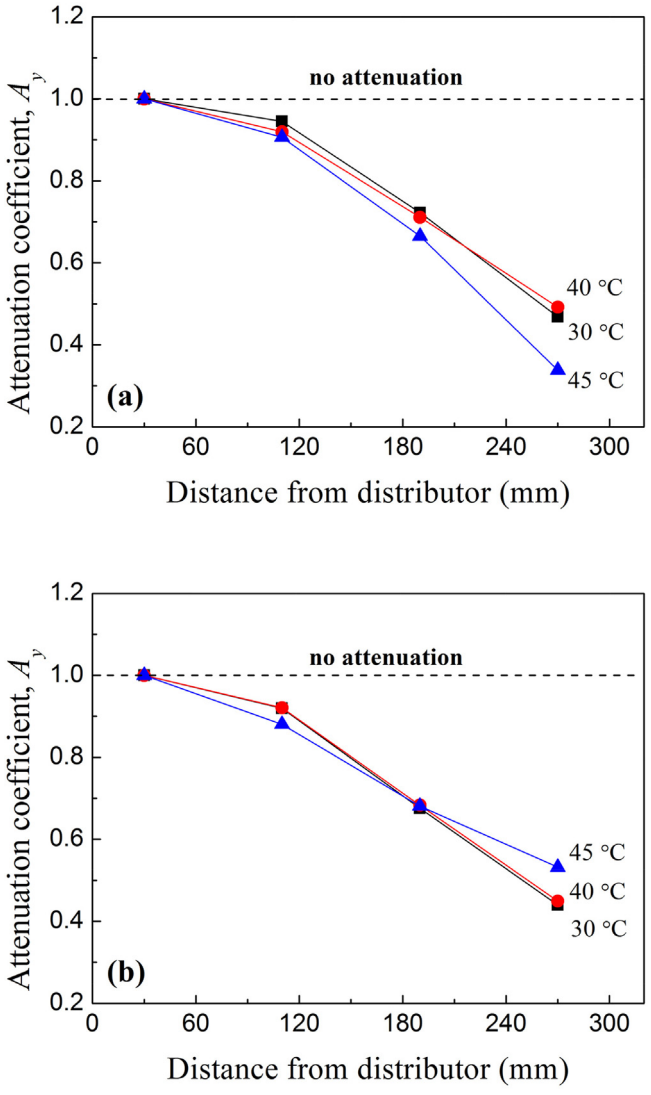

Fig. 11. Attenuation coefficients of pressure waves along the bed height under different cohesive forces at (a) $U_g = 2U_{mf}$; (b) $U_g = 3U_{mf}$.

Fig. 14 shows details about how to identify slugging for a time-series pressure signal collected at the bed temperature of 45 °C, $U_g = 2.5U_{mf}$, $H_s = 400$ mm and the measurement height of 30 mm. We first divide a signal of 10 min into 600 sections and calculated f_c for each section according to Eq.(2). Any section with f_c less than or equal to 2 Hz is identified as slugging. Based on this, the duration time of slugging (t_s) and normal fluidization (t_n) over a given period of time was collected by counting the number of respective sections, and the slugging time fraction, $\tau_{slugging}$, could be calculated as well:

$$\tau_{slugging} = \frac{t_s}{t_s + t_n} \tag{12}$$

Fig. 15 plots the effects of static bed height, H_s and inter-particle cohesive force on the slugging time fraction at the measurement height of 30 mm. For $H_s = 120$ mm and 200 mm, $\tau_{slugging}$ equals zero regardless of cohesive force, indicating that the whole-bed slugging hardly occurs throughout the cohesive forces studied. That is because the bubbles do not grow to an adequate size to trigger slugging due to the limitation of bed height. Therefore, reducing the static bed height can weaken or even avoid slugging under strong cohesive force. At $H_s = 300$ mm, the whole-bed slugging takes place due to the presence of large bubbles in the vicinity of bed surface and thus larger $\tau_{slugging}$ is observed. As the cohesive force increases, $\tau_{slugging}$ rises, mainly for two reasons: i)

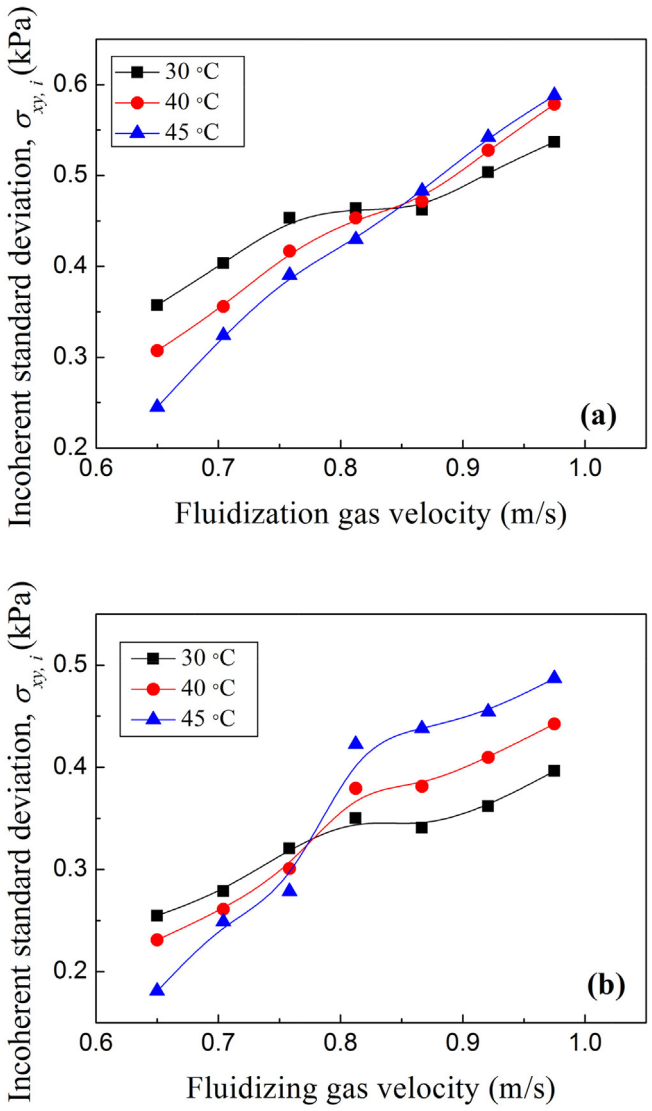

Fig. 12. Incoherent standard deviation as a function of fluidization gas velocity under different cohesive forces at the height of (a) 190 mm and (b) 270 mm.

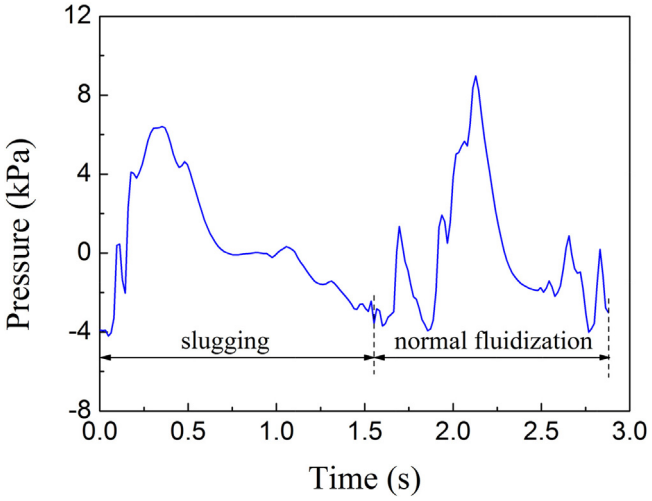

Fig. 13. Fragment of pressure signal. $U_g = 2.5U_{mf}$, $H_s = 400$ mm, bed temperature: 45 °C, measurement height: 30 mm.

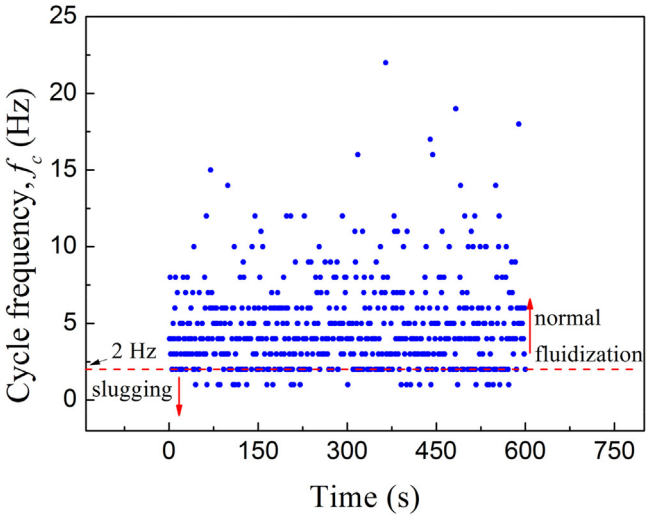

Fig. 14. Identification of slugging for a time-series pressure signal of 10 min. $U_g = 2.5U_{mf}$, $H_s = 400$ mm, bed temperature: 45 °C, measurement height: 30 mm.

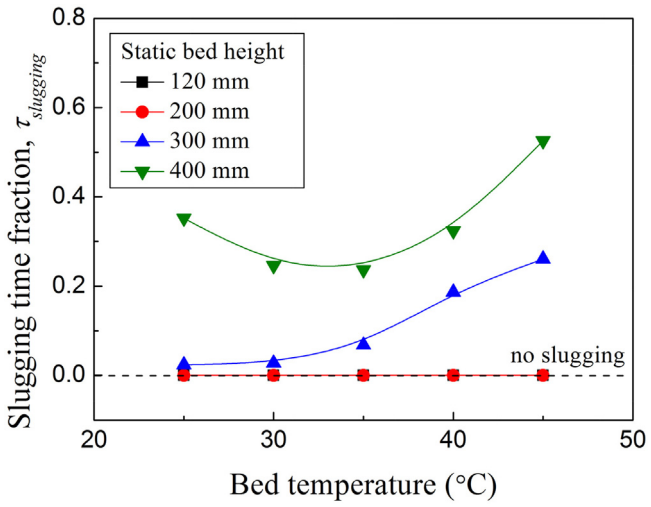

Fig. 15. Effects of static bed height on the slugging time fraction. Measurement height: 30 mm, $U_g = 2.5U_{mf}$.

increasing cohesive force enhances the size of bubbles, thus easier to induce slugging and causing an increase in $\tau_{slugging}$; ii) the slug stability increases with the cohesive force due to the enhanced bond between particles, thus increasing the lifetime of slug as well as $\tau_{slugging}$. Similar trends are also observed when $H_s = 400$ mm in which $\tau_{slugging}$ is the largest in comparison to other heights due to the full growth of bubbles near bed surface.

Fig. 16 shows the $\tau_{slugging}$ along the bed height at different fluidization gas velocities. The bed temperature maintains at 45 °C and $H_s = 300$ mm. $\tau_{slugging}$ increases with the measurement height and fluidization gas velocity. As previously analyzed, the slugging in a cohesive bed initially arises at upper bed then gradually extends toward the bottom. Therefore, the higher the measurement height, the larger $\tau_{slugging}$ is observed. According to the fluidization theory, the size of bubbles increases with the fluidization gas velocity [68]. Therefore, it is more prone to induce slugging and increase $\tau_{slugging}$ as well. Combining the results of Figs. 15 and 16, it can be concluded that any operations that promote bubble growth will facilitate the appearance of the whole-bed slugging under strong cohesive force.

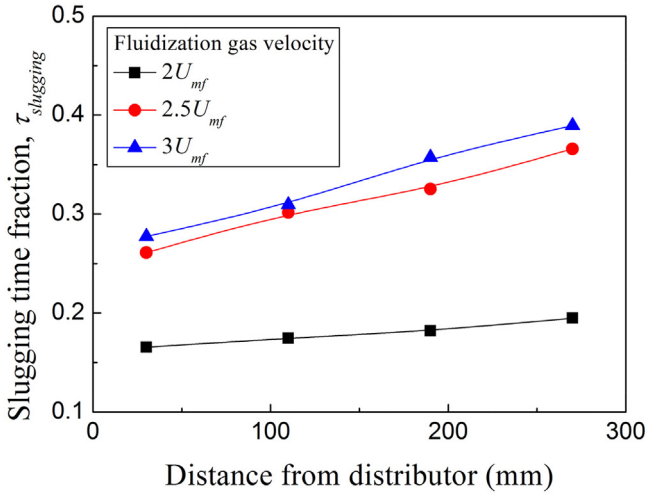

Fig. 16. Slugging time fraction along the bed height at different fluidization gas velocities for the temperature of 45 °C and the static bed height of 300 mm.

5. Concluding remarks

This paper studies the fluidization dynamics of cohesive Geldart B particles in a column by analyzing the in-bed pressure fluctuation signals. Various algorithms are applied to extract the key information underlying in the signals. With the aid of bubble dynamics reported in Part I, the local and global fluidization dynamics under different cohesive forces are discussed. The main conclusions are drawn as follows:

(1) Bulk bubble dynamics, i.e. formation, interaction, eruption of bubbles weakens with the presence of inter-particle cohesive force. As the cohesive force increases, the fluidization regime changes from multi-bubbling regime to single-bubble regime. The factor governing the pressure fluctuation changes from bubble formation to bubble eruption.
(2) Under strong cohesive force, slugging arises in the upper part of the bed, then gradually extends toward the bottom part of the bed by capturing freely fluidizing particles, and finally develops into the whole-bed slugging. At this time, regular fluidization turns into an alternative process between whole-bed slugging and regular status, corresponding to two distinct peaks in power spectral density of pressure signals at 0.1 Hz and 1 Hz respectively. Due to the frangibility of slugs, the size of gas slug decreases with the elevation of measurement height.
(3) Slugging can be identified by the reduction of cycle frequency below 2 Hz, indicating a deterioration of the bulk bubble dynamics. Any operations that promote bubble growth will facilitate the appearance of whole-bed slugging under strong cohesive force. Basically, reducing the static bed height is a preferable approach to weaken, or even avoid the defluidization of whole-bed slugging, without changing other operational parameters.

Acknowledgement

This work is supported by the National Natural Science Foundation of China (51806036) and the Natural Science Foundation of Jiangsu Province (BK20180398).

References

[1] Y. Zhou, C. Ren, J. Wang, Y. Yang, Characterization on hydrodynamic behavior in liquid-containing gas-solid fluidized bed reactor, AIChE J. 59 (2013) 1056–1065.
[2] Y. Zhou, Q. Shi, Z. Huang, J. Wang, Y. Yang, Particle agglomeration and control of gas-solid fluidized bed reactor with liquid bridge and solid bridge coupling actions, Chem. Eng. J. 330 (2017) 840–851.
[3] J. Shabanian, J. Chaouki, Effects of temperature, pressure, and interparticle forces on the hydrodynamics of a gas-solid fluidized bed, Chem. Eng. J. 313 (2017) 580–590.
[4] P.C. Wright, J.A. Raper, Role of liquid bridge forces in cohesive fluidization, Chem. Eng. Res. Des. 76 (1998) 753–760.
[5] H. Xu, W. Zhong, A. Yu, Z. Yuan, Spouting characteristics of wet particles in a conical-cylindrical spouted bed, Ind. Eng. Chem. Res. 54 (2015) 9894–9902.
[6] J. Gomez-Hernandez, A. Soria-Verdugo, J.V. Briongos, D. Santana, Fluidized bed with rotating distributor operated under defluidization conditions, Chem. Eng. J. 195 (2012) 198–207.
[7] M. Mokhtari, J. Chaouki, New technique for simultaneous measurement of the local solid and gas holdup by using optical fiber probes in the slurry bubble column, Chem. Eng. J. 358 (2019) 831–841.
[8] T. Wang, Y. He, T. Tang, W. Peng, Experimental and numerical study on a bubbling fluidized bed with wet particles, AIChE J. 62 (2016) 1970–1985.
[9] H. Xu, W. Zhong, Y. Shao, A. Yu, Experimental study on mixing behaviors of wet particles in a bubbling fluidized bed, Powder Technol. 340 (2018) 26–33.
[10] H. Che, H. Wang, J. Ye, W. Yang, Z. Wu, Application of microwave tomography to investigation the wet gas-solids flow hydrodynamic characteristics in a fluidized bed, Chem. Eng. Sci. 180 (2018) 20–32.
[11] C.M. Boyce, A. Penn, K.P. Pruessmann, C.R. Muller, Magnetic resonance imaging of gas-solid fluidization with liquid bridging, AIChE J. 64 (2018) 2958–2971.
[12] C. Savari, G. Kulah, M. Koksal, R. Sotudeh-Gharebagh, R. Zarghami, N. Mostoufi, Monitoring of liquid sprayed conical spouted beds by recurrence plots, Powder Technol. 316 (2017) 148–156.
[13] M. Mohagheghi, M. Hamidi, C. Briens, F. Berruti, J. McMillan, The effects of liquid properties and bed hydrodynamics on the distribution of liquid on solid fluidized particles in a cold-model fluidized bed, Powder Technol. 256 (2014) 5–12.
[14] C. Briens, H. Elkolaly, F. Berruti, J. McMillan, Effect of interactions between spray jets on liquid distribution in a fluidized bed, Can. J. Chem. Eng. 95 (2017) 680–687.
[15] A.H.A. Motlagh, J.R. Grace, C. Briens, F. Berruti, M. Farkhondehkavaki, M. Hamidi, Experimental analysis of volatile liquid injection into a fluidized bed, Particuology 34 (2017) 39–47.
[16] N. Prociw, C. Briens, F. Berruti, T. Jamaleddine, A method to measure the rate of liquid released from agglomerates produced by gas-atomized liquid injection into a fluidized bed, Measurement 125 (2018) 19–28.
[17] N. Prociw, C. Briens, F. Berruti, J. McMillan, Effect of spray nozzle attachment geometry on rate of liquid released from agglomerates produced by gas-atomized liquid injection into a fluidized bed, Powder Technol. 325 (2018) 280–288.
[18] J. Ma, J.R. van Ommen, D. Liu, R.F. Mudde, X. Chen, E.C. Wagner, C. Liang, Fluidization dynamics of cohesive Geldart B particles. Part I: X-ray tomography analysis, Chem. Eng. J. 359 (2019) 1024–1034.
[19] C. Rautenbach, R.F. Mudde, X. Yang, M.C. Melaaen, B.M. Halvorsen, A comparative study between electrical capacitance tomography and time-resolved X-ray tomography, Flow Meas. Instrum. 30 (2013) 34–44.
[20] J. van der Schaaf, J.C. Schouten, F. Johnsson, C.M. van den Bleek, Non-intrusive determination of bubble and slug length scales in fluidized beds by decomposition of the power spectral density of pressure time series, Int. J. Multiphase Flow. 28 (2002) 865–880.
[21] Y. Zhou, L. Yang, Y. Lu, X. Hu, X. Luo, H. Chen, Flow regime identification in gas-solid two-phase fluidization via acoustic emission technique, Chem. Eng. J. 334 (2018) 1484–1492.
[22] J.R. van Ommen, R.F. Mudde, Measuring the gas-solids distribution in fluidized beds-A review, Int. J. Chem. React. Eng. 6 (2008) 1–29.
[23] S. Sasic, B. Leckner, F. Johnsson, Time-frequency investigation of different modes of bubble flow in a gas-solid fluidized bed, Chem. Eng. J. 121 (2006) 27–35.
[24] Y. Zhang, H.T. Bi, J.R. Grace, C. Lu, Comparison of decoupling methods for analyzing pressure fluctuations in gas-fluidized beds, AIChE J. 56 (2010) 869–877.
[25] M. Rüdisüli, T.J. Schildhauer, S.M.A. Biollaz, A. Wokaun, J.R. van Ommen, Comparison of bubble growth obtained from pressure fluctuation measurements to optical probing and literature correlations, Chem. Eng. Sci. 74 (2012) 266–275.
[26] H. Ziaei-Halimejani, R. Zarghami, N. Mostoufi, Investigation of hydrodynamics of gas-solid fluidized beds using cross recurrence quantification analysis, Adv. Powder Technol. 28 (2017) 1237–1248.
[27] J. Wang, W. Zhong, H. Zhang, Characterization of flow regimes in fluidized beds by information entropy analysis of pressure fluctuations, Can. J. Chem. Eng. 95 (2017) 578–588.
[28] C.A.M. Silva, M.R. Parise, F.V. Silva, O.P. Taranto, Control of fluidized bed coating particles using Gaussian spectral pressure distribution, Powder Technol. 212 (2011) 445–458.
[29] J. Shabanian, P. Sauriol, J. Chaouki, A simple and robust approach for early detection of defluidization, Chem. Eng. J. 313 (2017) 144–456.
[30] L. de Martin, K. van den Dries, J.R. van Ommen, Comparison of three different methodologies of pressure signal processing to monitor fluidized-bed dryers/granulators, Chem. Eng. J. 172 (2011) 487–499.
[31] J.R. van Ommen, J.C. Schouten, C.M. van den Bleek, An early-warning-method for detecting bed agglomeration in fluidized bed combustors, 15th International Conference on Fluidized Bed Combustion, (1999).
[32] L. Luo, Y. Yan, P. Xie, J. Sun, Y. Xu, J. Yuan, Hilbert-Huang transform, Hurst and chaotic analysis based flow regime identification methods for an airlift reactor, Chem. Eng. J. 181–182 (2012) 570–580.
[33] O.A. Jaiboon, B. Chalermsinsuwan, L. Mekasut, P. Piumsomboon, Effect of flow pattern on power spectral density of pressure fluctuation in various fluidization regimes, Powder Technol. 233 (2013) 215–226.
[34] H.R. Norouzi, M. Tahmasebpoor, R. Zarghami, N. Mostoufi, Multi-scale analysis of flow structures in fluidized beds with immersed tubes, Particuology 21 (2015)

99–106.
[35] M. Abbasi, N. Mostoufi, R. Sotudeh-Gharebagh, R. Zarghami, A novel approach for simultaneous hydrodynamic characterization of gas-liquid and gas-solid systems, Chem. Eng. Sci. 100 (2013) 74–82.
[36] M. Bartels, J. Nijenhuis, F. Kapteijn, J.R. van Ommen, Detection of agglomeration and gradual particle size changes in circulating fluidized beds, Powder Technol. 202 (2010) 24–38.
[37] N. Ellis, L.A. Briens, J.R. Grace, H.T. Bi, C.J. Lim, Characterization of dynamic behaviour in gas-solid turbulent fluidized bed using chaos and wavelet analyses, Chem. Eng. J. 96 (2003) 105–116.
[38] T. Lichtenegger, Local and global recurrences in dynamic gas-solid flows, Int. J. Multiphase Flow 106 (2018) 125–137.
[39] F. Johnsson, R.C. Zijerveld, J.C. Schouten, C.M. van den Bleek, B. Leckner, Characterization of fluidization regimes by time-series analysis of pressure fluctuation, Int. J. Multiphase Flow 26 (2000) 663–715.
[40] J.R. van Ommen, S. Sasic, J. van der Schaaf, S. Gheorghiu, F. Johnsson, M.O. Coppens, Time-series analysis of pressure fluctuations in gas-solid fluidized beds-A review, Int. J. Multiphase Flow 37 (2011) 403–428.
[41] F. Karimi, R. Sotudeh-Gharebagh, R. Zarghami, N. Mostoufi, Monitoring the moisture content of solids in fluidized bed dryers by analysis of pressure fluctuations, Drying Technol. 29 (2011) 1697–1704.
[42] S. Bhowmick, N.A. Baveja, C.P. Shringi, K.T. Shenoy, S.K. Ghosh, Pressure fluctuations in a liquid-sprayed gas fluidized bed, Ind. Eng. Chem. Res. 53 (2014) 12631–12638.
[43] M. Bartels, J. Nijenhuis, J. Lensselink, M. Siedlecki, W. de Jong, F. Kapteijn, J.R. van Ommen, Detecting and counteracting agglomeration in fluidized bed biomass combustion, Energy Fuels 23 (2009) 157–169.
[44] Y. Zhou, Q. Shi, Z. Huang, J. Wang, Y. Yang, Effects of liquid action mechanisms on hydrodynamics in liquid-containing gas–solid fluidized bed reactor, Chem. Eng. J. 285 (2016) 121–127.
[45] Y. Zhou, Q. Shi, Z. Huang, Z. Liao, J. Wang, Y. Yang, Realization and control of multiple temperature zones in liquid-containing gas-solid fluidized bed reactor, AIChE J. 62 (2016) 1454–1466.
[46] J. Shabanian, J. Chaouki, Hydrodynamics of a gas-solid fluidized bed with thermally induced interparticle forces, Chem. Eng. J. 259 (2015) 135–152.
[47] J. Shabanian, J. Chaouki, Local characterization of a gas-solid fluidized bed in the presence of thermally induced interparticle forces, Chem. Eng. Sci. 119 (2014) 261–273.
[48] J. Shabanian, J. Chaouki, Fluidization characteristics of a bubbling gas–solid fluidized bed at high temperature in the presence of interparticle forces, Chem. Eng. J. 288 (2016) 344–358.
[49] H. Qiu, M. Bousmina, Determination of mutual diffusion coefficients at nonsymmetric polymer/polymer interfaces from rheometry, Macromolecules 33 (2000) 6588–6594.
[50] J. Shabanian, J. Fotovat, J. Chaouki, J. Bouffad, Fluidization behavior in a gas-solid fluidized bed with thermally induced inter-paticle forces, in: T. Knowlton (PSRI) (Ed.), 10th International Conference on Circulating Fluidized Beds and Fluidization Technology – CFB-10. ECI Symposium Series, New York, 2013, pp. 738–745.
[51] J. Bouffard, F. Bertrand, J. Chaouki, Control of particle cohesion with a polymer coating and temperature adjustment, AIChE J. 58 (2012) 3685–3696.
[52] C. Sobrino, S. Sanchez-Delgado, N. Garcia-Hernando, M. de Vega, Standard deviation of absolute and differential pressure fluctuations in fluidized beds of group B particles, Chem. Eng. Res. Des. 86 (2008) 1236–1242.
[53] J.R. van Ommen, R.J. de Korte, C.M. van den Bleek, Rapid detection of defluidization using the standard deviation of pressure fluctuations, Chem. Eng. Process. 43 (2004) 1329–1335.
[54] H. Bi, L.S. Fan, Existence of turbulent regime in gas-solid fluidization, AIChE J. 38 (1992) 297–301.
[55] M. Puncochar, J. Drahos, Origin of pressure fluctuations in fluidized beds, Chem. Eng. Sci. 60 (2005) 1193–1197.
[56] O. Trnka, V. Vesely, M. Hartman, Identification of the state of a fluidized bed by pressure fluctuations, AIChE J. 46 (2000) 509–514.
[57] H.T. Bi, A critical review of the complex pressure fluctuation phenomenon in gas-solids fluidized beds, Chem. Eng. Sci. 62 (2007) 3473–3493.
[58] Y. Zhang, J.R. Grace, X. Bi, C. Lu, M. Shi, Effect of louver baffles on hydrodynamics and gas mixing in a fluidized bed of FCC particles, Chem. Eng. J. 64 (2009) 3270–3281.
[59] B. Hao, H.T. Bi, Forced bed mass oscillations in gas-solid fluidized beds, Powder Technol. 149 (2005) 51–60.
[60] S. Sasic, B. Leckner, F. Johnsson, Fluctuations and waves in fluidized bed systems: the influence of the air-supply system, Powder Technol. 153 (2005) 176–195.
[61] M. Liu, Y. Zhang, H.T. Bi, J.R. Grace, Y. Zhu, Non-intrusive determination of bubble size in a gas-solid fluidized bed: an evaluation, Chem. Eng. Sci. 65 (2010) 3485–3493.
[62] J. van der Schaaf, J.C. Schouten, C.M. van den Bleek, Origin, propagation and attenuation of pressure waves in gas-solid fluidized beds, Powder Technol. 95 (1998) 220–233.
[63] H. Kage, M. Agari, H. Ogura, Y. Matsuno, Frequency analysis of pressure fluctuation in fluidized bed plenum and its confidence limit for detection of various modes of fluidization, Adv. Powder Technol. 11 (2000) 459–475.
[64] P. Cai, Z. Miao, Z. Yu, Y. Jin, Mathematic features and analysing methods of pressure fluctuation signal from a gas-solid fluidized bed, Eng. Chem. Metall. 11 (1990) 114–122.
[65] D. Musmarra, M. Poletto, S. Vaccaro, R. Clift, Dynamic waves in fluidized beds, Powder Technol. 82 (1995) 255–268.
[66] H.T. Bi, J.R. Grace, J. Zhu, Propagation of pressure waves and forced oscillations in gas-solid fluidized beds and their influence on diagnostics of local hydrodynamics, Powder Technol. 82 (1995) 239–253.
[67] M. Bartels, B. Vermeer, P.J.T. Verheijen, J. Nijenhuis, F. Kapteijn, J.R. van Ommen, Methodology for the screening of signal analysis methods for selective detection of hydrodynamic changes in fluidized bed systems, Ind. Eng. Chem. Res. 48 (2009) 3158–3166.
[68] J. Saayman, W. Nicol, J.R. van Ommen, R.F. Mudde, Fast X-ray tomography for the quantification of the bubbling-, turbulent- and fast fluidization-flow regimes and void structures, Chem. Eng. J. 234 (2013) 437–447.